Quasi-two-dimensional magnetism and antiferromagnetic ground state in Li_2FeSiO_4

W. Hergett,[1] N. Bouldi,[2] M. Jonak,[1] C. Neef,[1] C. Ritter,[3] M. Abdel-Hafiez,[1,4,5] F. Seewald,[6] H.-H. Klauss,[6] M. W. Haverkort,[2,*] and R. Klingeler[1,†]

[1]*Kirchhoff Institute of Physics, Heidelberg University, INF 227, D-69120 Heidelberg, Germany*
[2]*Institute for Theoretical Physics, Heidelberg University, D-69120 Heidelberg, Germany*
[3]*Institut Laue-Langevin, 38042 Grenoble, France*
[4]*Physics Department, Faculty of Science, Fayoum University, Fayoum 63514, Egypt*
[5]*Department of Applied Physics and Astronomy, University of Sharjah, P. O. Box 27272 Sharjah, United Arab Emirates*
[6]*Institute for Solid State and Materials Physics, TU Dresden, D-01069 Dresden, Germany*

(Received 5 November 2024; revised 18 December 2024; accepted 2 January 2025; published 17 January 2025)

Our experimental (neutron diffraction, Mössbauer spectroscopy, magnetic susceptibility, specific heat) and numerical studies on the evolution of short- and long-range magnetic order in γ_{II}-Li_2FeSiO_4 suggest a quasi-two-dimensional (2D) nature of magnetism. The experimental data obtained on single crystals imply long-range antiferromagnetic order below $T_N = 17$ K. A broad maximum in magnetic susceptibility χ at $T_m \simeq 28$ K, observation of magnetic entropy changes up to 100 K, and anisotropy in χ are indicative of low-dimensional magnetism and suggest short-range magnetic correlations up to 200 K. Neutron diffraction shows that long-range antiferromagnetic order is characterized by the propagation vector $\mathbf{k} = (\frac{1}{2}, 0, \frac{1}{2})$. The ordered moment $\mu = 2.50(2)\,\mu_B$/Fe, at $T = 1.5$ K, is along the crystallographic a axis. This is consistent with the observed static hyperfine field of $B_{hyp} = 14.8(3)$ T by Mössbauer spectroscopy which indicates significant orbital contributions. The temperature dependence of B_{hyp} yields the critical exponent $\beta = 0.116(12)$ which is in the regime of the 2D Ising behavior. LSDA + U studies exploiting the experimental spin structure suggest dominating magnetic exchange coupling within the ac layers (i.e., $J_3 \simeq -6$ K and $J_6 \simeq -2$ K) while interlayer coupling is much smaller and partly frustrated. This confirms the 2D nature of magnetism and is in full agreement with the experimental findings.

DOI: 10.1103/PhysRevB.111.024414

I. INTRODUCTION

The occurrence of magnetic order in low-dimensional and/or magnetically frustrated spin systems is directly linked to the interplay of magnetic interaction, geometric arrangement of the magnetic centers, and magnetic anisotropy. While in pure two-dimensional (2D) Heisenberg systems no long-range order is expected at finite temperature, observation of long-range magnetic order down to the monolayer in transition-metal-based van der Waals materials highlights the relevance of magnetic anisotropy in the evolution of a magnetic ground state (see, e.g., Ref. [1] and references therein). In particular in Jahn-Teller-active systems the orbital degree of freedom may be relevant, too, so that for example low-dimensional magnetism may be realized as observed in a variety of transition metal oxides [2–4]. Spin-orbit entanglement can yield magnetically and orbitally ordered ground states as observed, e.g., paradigmatically in systems such as $KCuF_3$ or $LaMnO_3$ and its doped variants [5–7]. The orthosilicate Li_2FeSiO_4 has been intensively studied in polycrystalline form as a high-capacity cathode material for lithium-ion batteries [8–10]. Its orthorhombic *Pmnb*-structured polymorph, γ_{II}-Li_2FeSiO_4, whose crystallographic unit cell is sketched in Fig. 1(a), exhibits tetrahedrally coordinated Fe^{2+} ions arranged in a layered structure where alternating layers of FeO_4/SiO_4 and LiO_4 tetrahedra are stacked along the b axis [11–13]. The distance between adjacent Fe^{2+} ions is 4.115(2) Å [black line in Fig. 1(b)], while the next-nearest neighbors are separated by 4.683(2) Å [red line in Fig. 1(b)]. Incidentally, both the nearest and next-nearest neighbors lie almost perfectly in the ac plane, with only a small displacement along the b axis, while Fe^{2+} ions are well separated along the b axis showing a nearest-neighbor distance of 5.339(3) Å. In tetrahedral coordination, $3d$ orbitals split into lower-lying e_g and higher-lying t_{2g} orbitals. The high-spin $S = 2$ configuration $e_g^3 t_{2g}^3$ of Fe^{2+} ions is Jahn-Teller (JT) active and implies the relevance of orbital degrees of freedom.

Here, we report the evolution of short- and long-range magnetic order in γ_{II}-Li_2FeSiO_4 single crystals and determine the magnetic ground state, which is characterized by the propagation vector $\mathbf{k} = (\frac{1}{2}, 0, \frac{1}{2})$. Our numerical studies, based on the experimental spin structure, imply dominating magnetic exchange coupling within the ac layers while interlayer coupling is small and partly frustrated. The numerically suggested quasi-two-dimensional nature of magnetism in Li_2FeSiO_4 is confirmed by our observation of a broad correlation-type maximum at $T_m \simeq 28$ K and of short-range magnetic correlations more than 10 times above the long-range antiferromagnetic ordering temperature $T_N = 17$ K.

*Contact author: haverkort@itp.uni-heidelberg.de
†Contact author: klingeler@kip.uni-heidelberg.de

II. EXPERIMENTAL AND NUMERICAL METHODS

Millimeter-sized single crystals of Li_2FeSiO_4 were grown by the high-pressure optical floating-zone method as described in detail in Refs. [14–16]. The thus-grown single crystals were oriented and cut into cuboids with approximate dimensions $1.1 \times 1.1 \times 1.0$ mm^3. Magnetization was studied in a Quantum Design MPMS-XL5 SQUID magnetometer. Specific-heat measurements were performed in a Quantum Design Physical Properties Measurement System (PPMS-14) using the relaxation method.

Polycrystalline samples of *Pmnb*-Li_2FeSiO_4 were synthesized by solid-state reaction as described in Ref. [15]. Phase purity was confirmed by x-ray diffraction (XRD), magnetic susceptibility, and powder neutron diffraction (PND). Li_2ZnSiO_4 was synthesized as a nonmagnetic analog to Li_2FeSiO_4 through a conventional solid-state reaction route, too. Stoichiometric amounts of Li_2CO_3, ZnO, and SiO_2 were mixed, ball-milled, calcined at 1100 °C, and characterized for phase purity by XRD. Neutron diffraction measurements on the powder sample of *Pmnb*-Li_2FeSiO_4 were obtained at several temperatures on the high-intensity D20 powder diffractometer at the Institut Laue-Langevin, Grenoble, France [17]. The sample, with a mass of approximately 1.6 g, was placed in a sealed vanadium can within a He cryostat. For both magnetic structure determination and nuclear structure refinement an incident neutron wavelength of 2.41 Å was used. Rietveld refinements of PND data were performed using the FullProf Suite program [18] and the magnetic symmetry analysis was performed by means of the program BasIreps [19], included in the FullProf Suite package. Sketches of the crystallographic and magnetic structures were drawn with the program VESTA [20].

^{57}Fe-Mössbauer (MB) measurements were performed on a powder sample from the same batch as studied by neutron diffraction and magnetization. The sample was mounted in a CryoVac helium flow cryostat using a commercial WissEL Mössbauer spectrometer. A ^{57}Co in Rh source driven in sinusoidal mode was used. Data evaluation was performed using the Mössfit software package [21] using a transmission integral analysis to account for the sample thickness. Measurements were carried out at temperatures ranging from 4.2 K to 296 K. All isomer shifts are reported relative to α-Fe at room temperature.

For the numerical studies, scalar relativistic first-principles calculations based on density functional theory (DFT) were performed by means of the package FPLO [22,23] (full potential local orbital) using the local density approximation (LDA) with the Perdew-Wang 92 parametrization [24] for the exchange correlation functional and periodic boundary conditions. FPLO is a code to solve the Kohn-Sham equation with a basis of atomic-like local orbitals within a full-potential approach. The experimental crystallographic structure (see Table I) was used for the calculations, and a Γ-centered k-point grid $8 \times 5 \times 10$ was set for the unit cell (4 Fe atoms).

To obtain the total energies associated with several magnetic configurations, we used the magnetic generalization of LDA with inclusion in the Fe-3d shell of the Hubbard term (LSDA + U) [25] with values for the Slater integrals $F^0 = 6.5$ eV, $F^2 = 10.1$ eV, and $F^4 = 6.2$ eV. To simulate antiferromagnetic structures, several supercells containing 8 iron atoms were built. We used the supercells $1 \times 1 \times 2$ and $2 \times 1 \times 1$ as well as a more unusual supercell of lattice parameters $\mathbf{a}' = 2\mathbf{a}$, $\mathbf{b}' = \mathbf{b}$, and $\mathbf{c}' = \mathbf{c} - \mathbf{a}$. The latter was needed to model the magnetic state obtained by neutron diffraction. In each case, the k-point grid was reduced according to the length multiplication.

TABLE I. Lattice parameters and atomic coordinates in the conventional unit cell for γ_{II}-Li_2FeSiO_4 used in the calculation (determined and refined by single-crystal x-ray diffraction) [15].

Li_2FeSiO_4, space group *Pmnb*				
$a = 6.27837$ Å; $b = 10.6290$ Å; $c = 5.03099$ Å				
		x	y	z
Li (8d)	1	0.494739	0.331319	−0.707234
Fe (4c)	.m.	0.750000	0.418512	−0.299501
Si (4c)	.m.	0.750000	0.583922	0.193420
O (4c)	.m.	0.750000	0.436406	−0.716996
O (4c)	.m.	0.750000	0.590409	−0.131224
O (8d)	1	0.461921	0.343885	−0.305747

III. EXPERIMENTAL RESULTS

A. Macroscopic properties of single crystals

Static magnetic susceptibility $\chi = M/B$ of Li_2FeSiO_4 exhibits anisotropic behavior up to the highest measured temperatures (see Figs. S1–S3 in the Supplemental Material (SM) [26]). This high-temperature anisotropy in χ is associated with the g tensor, as shown by scaling χ with axis-dependent g factors in Fig. 2. At high temperatures, χ reveals Curie-Weiss-like behavior, which is confirmed by quasilinear temperature dependence of the inverse volume susceptibility $\chi_{vol}^{-1} = 3/(\chi_a + \chi_b + \chi_c)$ at $T \gtrsim 200$ K (see the inset of Fig. 2). Analyzing the volume susceptibility in terms of a Curie-Weiss-like model, $\chi = N_A p^2 \mu_B^2 / 3k_B(T + \Theta) + \chi_0$, where N_A is Avogadro's number, μ_B is the Bohr magneton, and k_B is Boltzmann's constant, yields a Weiss temperature of $\Theta \approx 59(5)$ K and an effective magnetic moment of $p = 5.57(10)$ μ_B/f.u. The sign of Θ indicates predominant antiferromagnetic interactions. From the effective magnetic

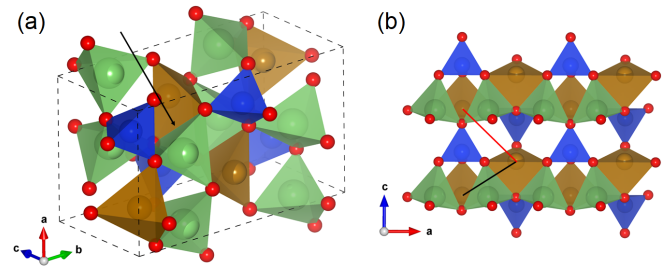

FIG. 1. (a) Crystallographic unit cell of γ_{II}-Li_2FeSiO_4, consisting of tetrahedra of LiO_4 (green), FeO_4 (brown), and SiO_4 (blue). Oxygen ions are depicted in red. The black arrow points to the edge shared by the FeO_4 and LiO_4 tetrahedra. (b) Cross section of the *ac* plane. The black and red lines mark the shortest and second-shortest magnetic bonds, respectively.

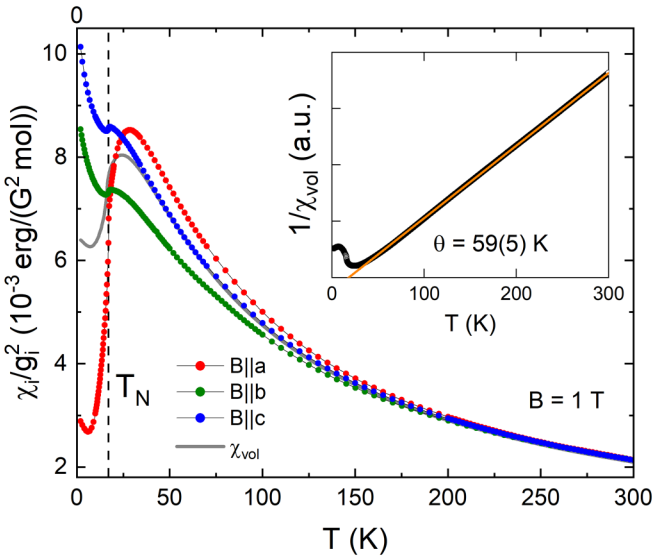

FIG. 2. Static magnetic susceptibility, $\chi_i = M_i/B_i$ $(i = a, b, c, \text{vol})$, obtained at $B = 1$ T, divided by axis-dependent g factors, g_i, as a function of temperature. The dashed vertical line marks T_N. Inset: Inverse of the volume susceptibility, χ_{vol}, vs temperature at $B = 5$ T. The orange line represents a fit using a Curie-Weiss model (see the text).

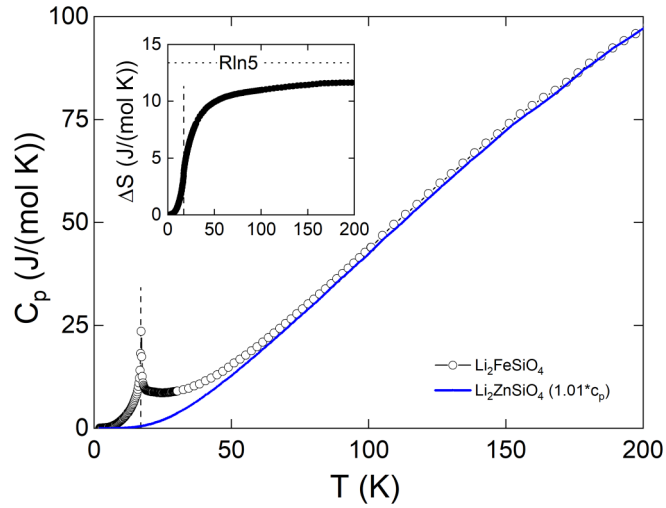

FIG. 3. Specific-heat capacity, c_p, of Li_2FeSiO_4 (black symbols) and Li_2ZnSiO_4 (blue line, scaled by a factor of 1.01) at $B = 0$ T vs temperature. (a) c_p vs T^3 (see also Fig. S4 in the SM [26]). Inset: Magnetic entropy changes, ΔS, obtained by integrating c_p^m/T, where $c_p^m = c_p(Li_2FeSiO_4) - 1.01 \times c_p(Li_2ZnSiO_4)$. Dashed vertical lines mark T_N.

moment, the tetrahedrally coordinated Fe^{2+} ions are deduced to be in the high-spin $S = 2$ state, suggesting an electronic configuration of $3e_g^3t_{2g}^3$. We conclude the volume g factor $g_{vol} = 2.27(1)$ which is in the upper range of typical values of tetrahedrally coordinated Fe^{2+} [27–29]. From the uniaxial susceptibilities we read off $g_a = 2.36(1)$, $g_b = 2.19(1)$, and $g_c = 2.28(1)$.

Upon cooling, magnetic anisotropy beyond the g-tensor anisotropy appears below $T \approx 200$ K. A sharp decrease of χ at low temperatures implies the onset of long-range antiferromagnetic order with the crystallographic a direction being the magnetic easy axis. In addition, for $B \| a$ there is a broad maximum in χ_a at around $T_m = 28$ K while the onset of long-range antiferromagnetic order is signaled by a sharp downturn in χ_a and a λ-like anomaly in the magnetic specific heat, $\partial(\chi_a T)/\partial T$ (see Figs. 2 and 4). These data imply $T_N = 17.0(5)$ K which is similar to previous studies on polycrystalline Li_2FeSiO_4 [30–32]. For $B \perp a$, the magnetic susceptibility displays much smaller anomalies at T_N. A Curie-like upturn at lowest temperatures indicates the presence of approximately 0.5% of only weakly correlated magnetic moments that do not participate in long-range antiferromagnetic spin order and may be considered "quasifree." The presence of quasifree moments is also confirmed by the initial Brillouin-like right-bending observed in the M vs B curves (see Fig. S4 in the SM [26]). A small fraction of quasifree Fe^{2+} moments is expected due to defects which may in particular be Li-Fe antisite defects which arise from similar covalent radii of Li and Fe ions [15,33,34]. These antisite defects typically exhibit an anisotropic nature, as reflected by the fact that signatures of quasifree moments in $M(T)$ and $M(B)$ are much weaker for B applied along the a axis. Our data indicate a g factor anisotropy of the quasifree moments of $g_b^{qf} \simeq g_c^{qf} \simeq 4g_a^{qf}$.

The comparison of the specific heat of Li_2FeSiO_4 and its compositionally and structurally similar nonmagnetic counterpart Li_2ZnSiO_4, as shown in Fig. 3, demonstrates the predominant phononic nature of entropy changes at high temperatures. The phononic specific heat is superimposed by a pronounced λ-shaped anomaly which signals a continuous phase transition to a long-range-ordered ground state at T_N. The specific heat of Li_2ZnSiO_4 enables assessing the magnetic specific heat $c_p^m = c_p(Li_2FeSiO_4) - 1.01 \times c_p(Li_2ZnSiO_4)$. As shown in Fig. 4, the so-obtained magnetic specific heat c_p^m scales excellently with Fisher's specific heat $\partial(\chi_a T)/\partial T$ which confirms the validity of our

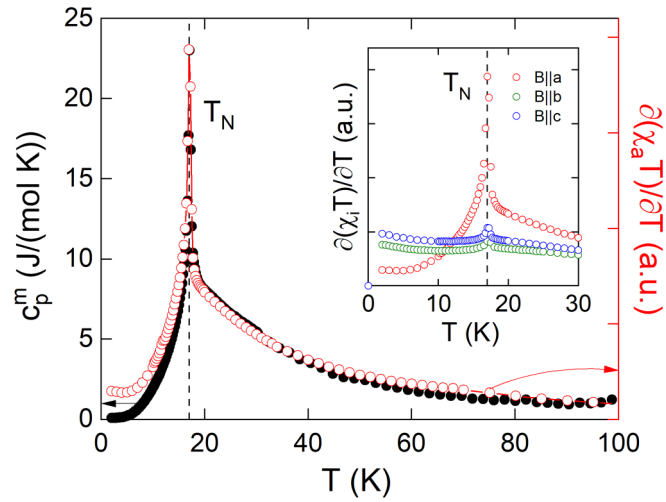

FIG. 4. Magnetic specific heat, c_p^m (left axis), obtained by subtracting the specific heat of nonmagnetic Li_2ZnSiO_4 from the data for Li_2FeSiO_4 (see Fig. 3), and the derivative $\partial(\chi_a T)/\partial T$ of the static magnetic susceptibility, i.e., Fisher's specific heat (right axis). Inset: Fisher's specific heat for all crystallographic axes.

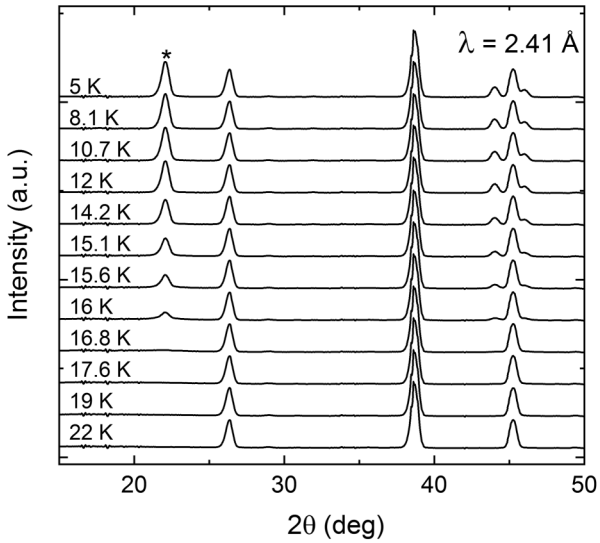

FIG. 5. Neutron diffractograms at various temperatures between 5 and 22 K. The asterisk labels the (010) magnetic peak (and equivalents) used for determining the temperature dependence of sublattice magnetization shown in Fig. 7.

analysis. Comparison of the data implies significant magnetic entropy changes at least up to 100 K. Integrating c_p^{m}/T yields magnetic entropy changes $\Delta S(T)$, as shown in Fig. 3(b). Quantitatively, the obtained magnetic entropy changes saturate at $\Delta S_{\mathrm{tot}} \approx 11.7(2)$ J/(mol K) which falls within the theoretical prediction $R\ln(2S+1) \approx 13.4$ J/(mol K). Nearly half of the measured entropy changes appear above T_{N}, while 6.7 J/(mol K) are released in the temperature regime 2 K $\leqslant T \leqslant T_{\mathrm{N}}$.

B. Neutron diffraction

Powder neutron diffraction (PND) in the temperature range between 1.5 and 25 K was performed to investigate the nuclear and magnetic structure at low temperatures. A detailed description of the full crystal structure determination and refinement of the investigated *Pmnb*-Li_2FeSiO_4 polymorph, achieved via single-crystal x-ray diffraction, is provided in Ref. [15]. The diffraction profiles in the 2θ range 10°–50° are displayed in Fig. 5 for selected temperatures [17]. The PND patterns indicate the evolution of superstructure reflections below 16.8 K. As the temperature decreases, the intensity of the superstructure peaks increases, while their positions remain unchanged in the measured temperature range. The appearance of additional Bragg reflections (one exemplary peak is labeled by the asterisk in Fig. 5) at angles smaller than the angular position of the first nuclear reflection at 26.3° confirms the presence of long-range antiferromagnetic spin order at low temperatures, consistent with the macroscopic data presented above. By indexing the corresponding Bragg reflections, a magnetic propagation vector $\mathbf{k} = (\frac{1}{2}, 0, \frac{1}{2})$ is found. We conclude that the magnetic structure is commensurate with the nuclear lattice. The magnetic unit cell is double the crystallographic one in both the *a*- and *c*-axis directions, while it is the same in the *b*-axis direction. Consequently, there are 16 Fe ions in the magnetic unit cell, while the crystallographic unit cell contains 4 Fe ions. For the space group *Pmnb* and for $\mathbf{k} = (\frac{1}{2}, 0, \frac{1}{2})$, the magnetic reducible representation Γ_{mag} for the Fe^{2+} (4c) site decomposes as a direct sum of two nonzero irreducible representations (IRs):

$$\Gamma_{\mathrm{mag}} = 3\Gamma_1^2 \oplus 3\Gamma_2^2. \quad (1)$$

The basis vectors of these IRs are listed in Table II. Of the two allowed antiferromagnetic spin configurations, only Γ_1 can reproduce the measured magnetic intensities. The resulting spin configuration is visualized in Fig. 6. The magnetic moments of Fe^{2+} are aligned antiferromagnetically along the *a* axis with an ordered moment of 2.50(2) μ_{B}/Fe at $T =$ 1.5 K. Its magnitude is smaller than the expected value of ~4.5 μ_{B} for magnetic moment of Fe^{2+} (considering the measured $g = 2.27$) in the high-spin $S = 2$ state.

Figure 7 shows the integrated intensity ($I_B \propto |M_s|^2$, where M_s is the order parameter) of the strongest magnetic peak (010) in the temperature range 2–19 K. The intensity vanishes around T_{N}, which agrees with the specific-heat data. In the conventional picture of a continuous phase transition, the magnetic order parameter follows a power-law equation. By fitting the integrated intensity to the power-law scaling

TABLE II. Basis vectors of the two irreducible representations for Li_2FeSiO_4 with space group *Pmnb* and $\mathbf{k} = (\frac{1}{2}, 0, \frac{1}{2})$ propagation vector obtained from representational analysis. Fe-1, Fe-2, Fe-3, and Fe-4 refer to the nonprimitive basis with coordinates (0.75, 0.42, 0.7), (−0.75, 0.08, 1.2), (1.25, −0.42, −0.7), and (−0.25, 0.92, −0.2), respectively. The magnetic *R* value (R_{mag}) for the refinement based on Γ_1 yields a satisfactorily low value of 4.73%, while the magnetic ordering schema associated with the Γ_2 representation is ruled out, as it is incapable of simulating the observed magnetic reflections.

IR	Ψ_ν	Component	Fe-1	Fe-2	Fe-3	Fe-4
Γ_1	Ψ_1	Re	(100)	(000)	(000)	(−100)
		Im	(000)	(100)	(−100)	(000)
	Ψ_2	Re	(010)	(000)	(000)	(010)
		Im	(000)	(010)	(010)	(000)
	Ψ_3	Re	(001)	(000)	(000)	(00−1)
		Im	(000)	(00−1)	(001)	(000)
	Ψ_4	Re	(000)	(−100)	(100)	(000)
		Im	(−100)	(000)	(000)	(100)
	Ψ_5	Re	(000)	(010)	(010)	(000)
		Im	(010)	(000)	(000)	(010)
	Ψ_6	Re	(000)	(00−1)	(001)	(000)
		Im	(001)	(000)	(000)	(00−1)
Γ_2	Ψ_1	Re	(100)	(000)	(000)	(100)
		Im	(000)	(100)	(100)	(000)
	Ψ_2	Re	(010)	(000)	(000)	(0−10)
		Im	(000)	(010)	(0−10)	(000)
	Ψ_3	Re	(001)	(000)	(000)	(001)
		Im	(000)	(00−1)	(00−1)	(000)
	Ψ_4	Re	(000)	(100)	(100)	(000)
		Im	(100)	(000)	(000)	(100)
	Ψ_5	Re	(000)	(0−10)	(010)	(000)
		Im	(0−10)	(000)	(000)	(010)
	Ψ_6	Re	(000)	(001)	(001)	(000)
		Im	(00−1)	(000)	(000)	(00−1)

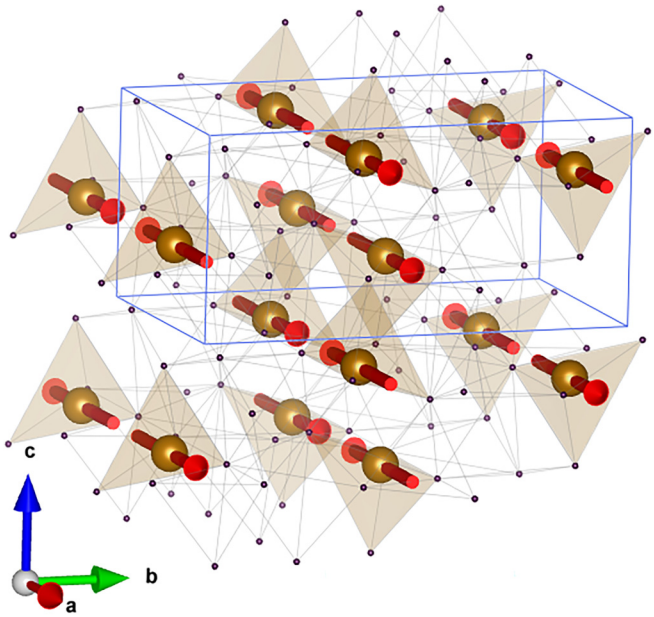

FIG. 6. Sketch of the spin configuration. Lines show the crystallographic unit cell.

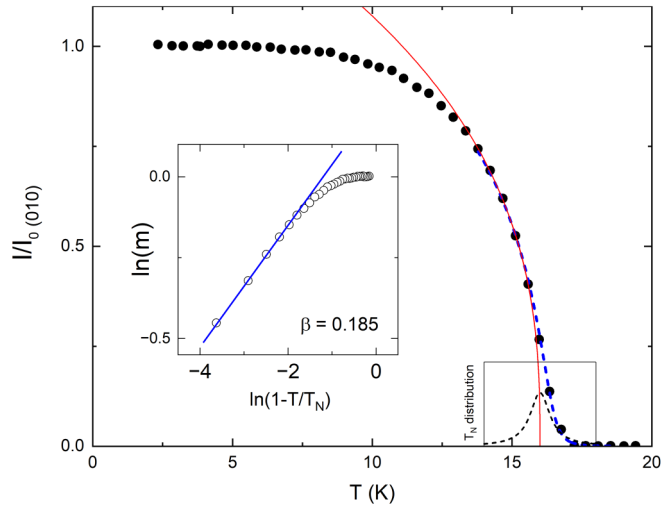

FIG. 7. Order parameter fit analysis of the intensity of the (010) magnetic superstructure reflection (see Fig. 5). The solid red line represents a fit to the data by a power law and the blue dashed line the fit by Eq. (2), i.e., by considering the variation of the Néel temperature as shown by the black short-dashed line (see the text). The inset shows a logarithmic plot of the sublattice magnetization as a function of the reduced temperature. The solid blue line in the inset represents a fit obtained with the critical exponent $\beta = 0.185$.

function $I_B = I_0|t|^{2\beta}$, where $t = 1 - T/T_N$ is the reduced temperature, an estimate for the critical exponent $\beta = 0.18(2)$ is obtained.[1] As will be discussed below, we interpret the thus obtained power-law exponent only as an effective value describing a convolution of temperature dependence of the order parameter and of the magnetic volume fraction; i.e., it does not directly reflect the critical behavior (see Sec. III C).

In the vicinity of T_N the temperature dependence of the order parameter is not very well described by a power law which would yield a sharp kink at T_N instead of the observed smeared-out behavior (see Fig. 7). A better fit is obtained by assuming a Lorentzian distribution of T_N which may result from strain effects or tiny variations of oxygen content in the sample. Assuming the distribution of T_N with full width at half maximum (FWHM) around a center Néel temperature T_N^{cen} in the measured polycrystal, the fit to the data is obtained by performing a convolution of the power-law scaling function

$$f(T_N) = f_0\left[\frac{\gamma}{\left(T_N - T_N^{cen}\right)^2 + \gamma^2}\right]. \quad (2)$$

Here, f_0 is a normalization prefactor, and γ is the scale parameter, which determines the FWHM $= 2\gamma$. The resultant fit is shown by the dashed blue line in Fig. 7, with $T_N^{cen} = (16.02 \pm 0.02)$ K and $\gamma = (0.43 \pm 0.05)$ K.

C. Mössbauer spectroscopy

Representative Mössbauer spectra of Li_2FeSiO_4 are shown in Fig. 8. All spectra are analyzed using a static nuclear hyperfine Hamiltonian for powder samples. At $T = 4.2$ K, two Fe sites are observed. The main site has an intensity fraction of $a_1 = 95.6(6)\%$ and is characterized by an electric field gradient (EFG) as well as a magnetic hyperfine field of $B_{hyp} = 14.8(3)$ T. The principal EFG component of $V_{zz} = -127.3(8)$ V/Å^2 is orientated orthogonal to the magnetic hyperfine field, which is parallel to its smallest principal axis V_{yy} with the three principle axes of the EFG given by $|V_{zz}| \geqslant |V_{yy}| \geqslant |V_{xx}|$. The EFG shows an asymmetry parameter $\eta = (V_{yy} - V_{xx})/V_{zz} = 0.752(8)$. The main site exhibits an isomer shift $\delta = 1.109(10)$ mm/s. The second site with an relative intensity of $a_2 = 4.4(6)\%$ shows a magnetic hyperfine field of $B_{hyp} = 23.5(10)$ T with an isomer shift of 0.5(2) mm/s.

At room temperature, the spectra imply the presence of two sites, too [see Fig. 8(d)]. For the main site [relative intensity $a = 94.7(30)\%$] the asymmetry parameter η obtained from the low-temperature spectrum at 4.2 K is assumed. This site shows a quadruple-splitting with an EFG principal component of $V_{zz} = -124.8(20)$ V/Å^2, similar to the data at 4.2 K. The isomer shift is $\delta = 0.96(1)$ mm/s. The minority site with a relative intensity of $a = 5.3(30)\%$ is described by a broadened singlet (i.e., EFG $\approx$0) with an isomer shift of $\delta = 0.42(10)$ mm/s. This site may be associated with excess iron ions on an interstitial position in the unit cell.

The isomer shift of $\delta = 0.96(1)$ mm/s for the main site at room temperature in combination with the EFG value unambiguously confirms the Fe^{2+} ($S = 2$) high-spin state in Li_2FeSiO_4. The finite value of the EFG asymmetry parameter η is in agreement with the distorted tetrahedral crystal field around the Fe nucleus [15].

Between room temperature and 20 K the Mössbauer spectra show no static hyperfine field which is consistent with a paramagnetic state. Below 20 K a magnetic phase transition is observed via the gradual appearance of a static magnetic hyperfine field B_{hyp}. For all temperatures below T_N the angle ϑ

[1]For fitting the data, we used $T_N = 16$ K, as determined from characterizing the powder sample used for the neutron study.

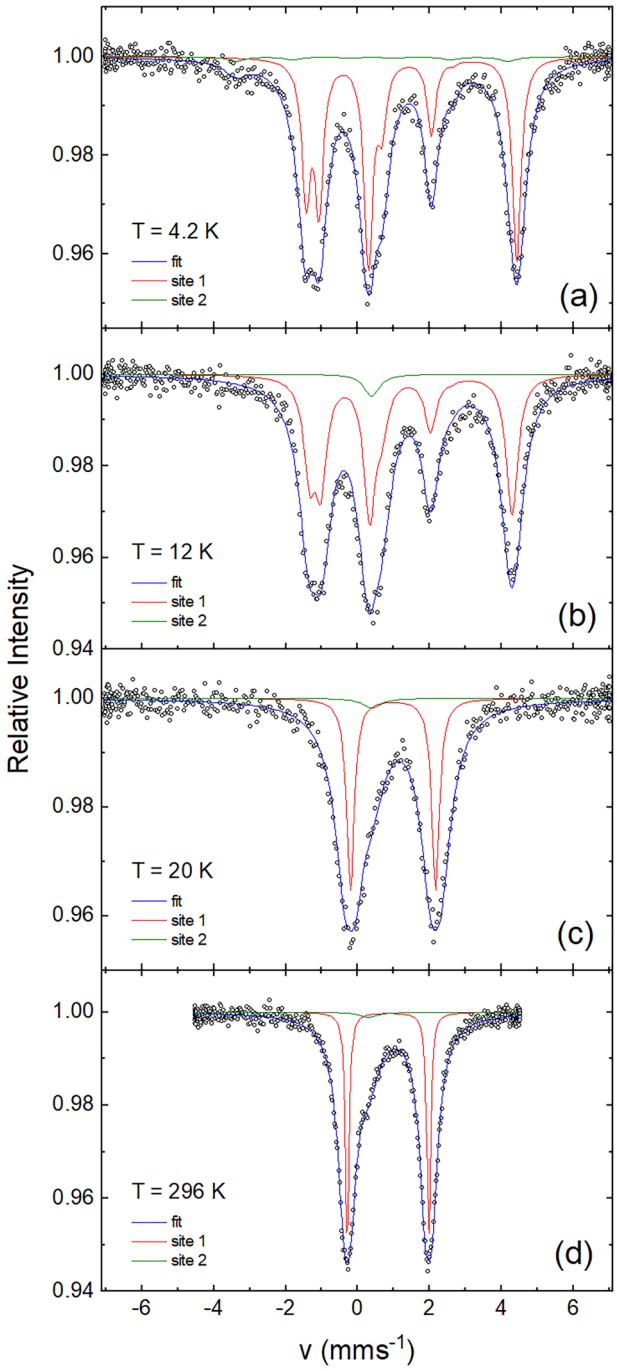

FIG. 8. Typical Mössbauer spectra of Li_2FeSiO_4 at 4.2, 12, 20, and 296 K. The spectra can be described by a static hyperfine Hamiltonian analysis (blue) assuming two magnetic sites. The main site (red) exhibits an electric field gradient as well as a static hyperfine field below 20 K. Site 2 contributes with ≈5%. It exhibits a singlet above 4.2 K and shows a static magnetic hyperfine field at 4.2 K.

between V_{zz} and B_{hyp} determined from the Mössbauer spectra analysis is 90(2) degrees. The orientation of V_{zz} orthogonal to B_{hyp} is in agreement with the iron magnetic moment orientation parallel to the undistorted tetrahedral axis as deduced from macroscopic magnetization and neutron powder diffraction as discussed above.

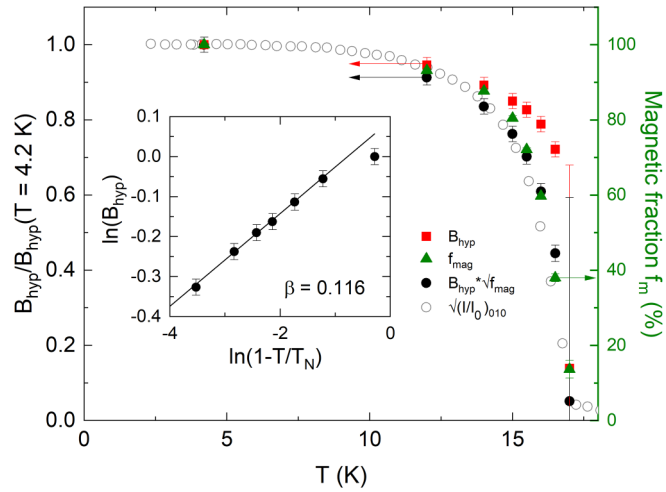

FIG. 9. Temperature dependence of the normalized magnetic hyperfine field B_{hyp} below 20 K (red squares, left ordinate) and of the magnetic volume fraction f_{mag} determined from the analysis of the Mössbauer spectra (green triangles, right ordinate). The black solid circles describe the product $B_{hyp} \times \sqrt{f_{mag}}$ and the black open circles describe $\sqrt{I_{010}}$ from Fig. 7 (all normalized to their low-temperature values). The inset shows a double-logarithmic plot of B_{hyp} as a function of the reduced temperature.

The temperature dependence of B_{hyp}, which is proportional to the magnetic order parameter M_s, is shown in Fig. 9 (solid red squares). For comparison, we include the scaled temperature dependence of the neutron magnetic order parameter M_s from Fig. 7 (black open circles). Below 13 K both data sets are following the same trend. However, between 14 and 17 K the Mössbauer hyperfine field B_{hyp} is always above the corresponding neutron value.

This discrepancy is not expected for three-dimensional magnets (see, e.g., Ref. [35] and references therein). In the local-probe Mössbauer spectroscopy the determination of the temperature-dependent magnetic order parameter $B_{hyp}(T)$ is independent of the magnetic volume fraction $f_{mag}(T)$ determined from the signal intensity. In contrast, the neutron diffraction magnetic order parameter obtained from the intensity of a magnetic Bragg peak, i.e., $\sqrt{I_{010}(T)}$, is proportional to the static magnetic dipole moment $M_s(T)$ multiplied by the square root of $f_{mag}(T)$. The continuous decrease of $f_{mag}(T)$ from 1 to 0 in the vicinity of the magnetic phase transition (determined from the analysis of the Mössbauer spectra and shown in Fig. 9, right ordinate) leads to the suppression of the neutron magnetic order parameter in this temperature range. For illustration in Fig. 9 we also include a plot of the product $B_{hyp}(T) \times \sqrt{f_{mag}(T)}$ (filled black circles). These data are in very good approximation proportional to the experimental values of $\sqrt{I_{010}(T)}$.

The inset of Fig. 9 shows a logarithmic plot of $B_{hyp}(T)$ as a function of the reduced temperature. The solid blue line represents a fit obtained with the critical exponent $\beta = 0.116(12)$ and $T_N^{MB} = 17$ K. Since $B_{hyp}(T)$ is directly proportional to $M_s(T)$ this value of β may be considered as the thermodynamic critical exponent of the magnetic phase transition in Li_2FeSiO_4.

TABLE III. Comparison of Mössbauer hyperfine parameters for Li_2FeSiO_4 (this work) with those of Cu_2FeGeS_4 (Ref. [37]). B_{hyp}, V_{zz}, ϑ, and η are the magnetic hyperfine field, the principal component of the EFG, the angle between V_{zz} and B_{hyp}, and the asymmetry parameter as discussed in the text.

	B_{hyp} (T)	V_{zz} (V/Å^2)	ϑ (deg)	η
Li_2FeSiO_4	14.8(3)	−127.3(8)	90(2)	0.752(8)
Cu_2FeGeS_4	16.7(2)	−151.8(18)	90(1)	0.00(3)

Next we discuss the absolute value of the iron Mössbauer magnetic hyperfine field $B_{hyp} = 14.8(3)$ T at the lowest measured temperature of $T = 4.2$ K. This value is consistent with the absolute value of the ordered dipole moment of 2.5 μ_B as determined by our neutron diffraction experiment. In a magnetic insulator B_{hyp} is given by [36]

$$B_{hyp} = B_s + B_L + B_D, \tag{3}$$

where B_s is the Fermi contact field being typically in the range of 20–50 T for high-spin Fe^{2+}. B_L is the orbital field which is usually of the order of 20 T and antiparallel to B_s. B_D is the dipole field usually at the order of a few teslas for iron [36]. The measured B_{hyp} hence suggests the presence of a measurable orbital contribution to the local hyperfine field and hence to the magnetic order parameter.

In Table III the Mössbauer hyperfine parameters of Li_2FeSiO_4 are compared to those for high-spin Fe^{2+} in the structurally similar compound Cu_2FeGeS_4 analyzed in Ref. [37]. In both systems, magnetism is associated with tetrahedrally coordinated iron sites. A main difference between both materials is that the tetrahedra in Cu_2FeGeS_4 are not distorted in contrast to what is observed in Li_2FeSiO_4[15]. Accordingly, η is found to vanish in Cu_2FeGeS_4 whereas the distorted tetrahedral environment in the *bc* plane of Li_2FeSiO_4 results in $\eta = 0.752(8)$.

IV. NUMERICAL STUDIES

The magnetic coupling parameters were obtained by comparison of the DFT + U calculated total energies for several magnetic configurations. This approach, sometimes called "broken-symmetry formalism" [38,39], is quite common in the literature [40,41]. Individual exchange couplings J_l were defined by the spin Hamiltonian $\sum_{\langle i,j\rangle} J_l \mathbf{S_i}\mathbf{S_j}$, where i and j are lth neighbors, $\mathbf{S_i}$ are the spin operators located on site i divided by $\hbar$ ($\mathbf{S_i}$ is dimensionless), and J_l are the magnetic exchange coupling between lth neighbors (J_l are energies). Here, we have included six nearest neighbors as depicted in Fig. 10. The corresponding distances are listed in Table IV.

We studied the ferromagnetic (FM) configuration and 21 different antiferromagnetic (AFM) configurations that we label $\alpha \in [1, \ldots, 21]$. All DFT + U self-consistent field calculations converged to structures in which the magnetic moment per atom is 1.87 μ_B at all sites. For a given configuration the Heisenberg Hamiltonian can therefore be rewritten as a linear combination of J_l with dimensionless coefficients c_l^α which only depend on the spins on the bond being parallel

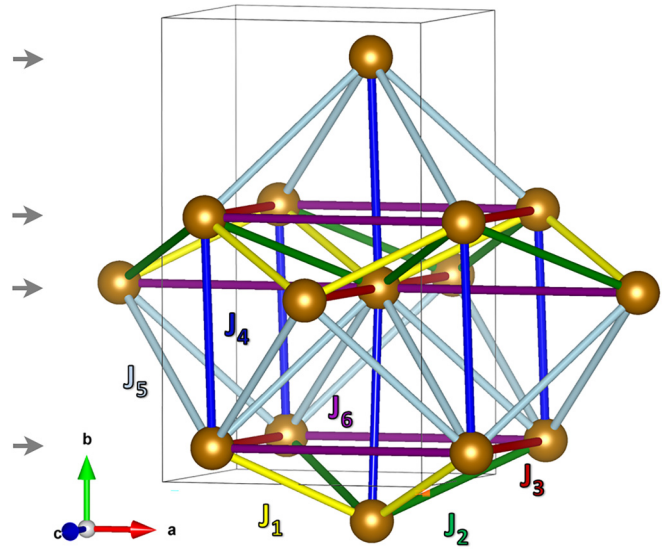

FIG. 10. Illustration of the magnetic interactions between Fe^{2+} moments which have been considered in the model (up to the 6th nearest neighbor). Thin black lines show the crystallographic unit cell. Four horizontal gray arrows on the left indicate the successive Fe layers stacked along the *b* direction within the shown unit cell.

($c_l = 1$) or antiparallel ($c_l = -1$) in the configuration:

$$-\sum_{\substack{\langle i,j\rangle \\ l\text{th neighbor}}} J_l \mathbf{S_i}\mathbf{S_j} = -\sum_{l=1}^{6} J_l^{DFT} c_l^\alpha. \tag{4}$$

For the ferromagnetic configuration, all the c_l are equal to +1 while for AFM structures they are either +1 or −1 depending on the relative spin orientation on the bond.

In Fig. 11, the energy $E_{DFT}^\alpha - E_{DFT}^{FM}$ is plotted against $\sum_{l=1}^{6}(c_l^\alpha - 1)J_l M_S^2$ for the 21 different antiferromagnetic configurations. The calculated energy of the experimental antiferromagnetic configuration as determined by neutron diffraction is represented in orange. In our calculations, it is almost the lowest energy configuration. Using the LeastSquares function of Mathematica [42], we determined the values of J_l

TABLE IV. Coupling constants and corresponding Fe-Fe distances d_{Fe-Fe}: J^{DFT} are the raw solutions in meV and $J_L = J^{DFT}/S(S+1) = J^{DFT}/6$ are the actual coupling constants. It is important to note that, because of the driving role of J_3 and J_6 (see text), the values obtained for all other J_l are subject to a large relative uncertainty.

	d_{Fe-Fe} (Å)		J^{DFT} (meV)	J_L (K)
J_1	4.114		-2.2×10^{-3}	−0.004
J_2	4.684		-2.6×10^{-1}	−0.50
J_3	5.031	$\|\|\,\mathbf{c}$	−3.2	−6.1
J_4	5.338	almost $\|\|\,\mathbf{b}$	2.5×10^{-1}	0.48
J_5	5.387		-3.5×10^{-2}	−0.068
J_6	6.278	$\|\|\,\mathbf{a}$	−0.9	−1.74

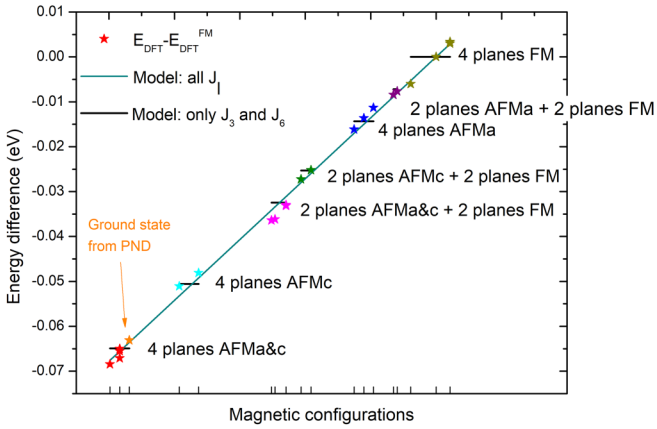

FIG. 11. Total energies computed for several antiferromagnetic spin configurations compared with the values obtained with the Heisenberg model Eq. (4). For clarity, magnetic configurations are spread along the x axis so that $\sum_{l=1}^{6} c_l^{\alpha} J_l^{\mathrm{DFT}}$ appears to be linear. The star scatters depict the DFT-calculated total energy for a given magnetic structure minus the calculated total energy for the ferromagnetic structure. The cyan line corresponds to $\sum_{l=1}^{6} -(c_l^{\alpha} - 1)J_l^{\mathrm{DFT}}$ with the values for J_l listed in Table IV. The black lines depict the model Hamiltonian considering only J_3 and J_6 as nonzero. Abbreviations (see also Fig. 12): AFMi (&j) = AFM alignment of neighboring moments in direction(s) i (&j) and FM alignment along the other in-plane direction.

that minimize the quantity

$$\sum_{\alpha} \left[\left(E_{\mathrm{DFT}}^{\alpha} - E_{\mathrm{DFT}}^{\mathrm{FM}} \right) - \sum_{l=1}^{6} \left(c_l^{\alpha} - 1 \right) J^{\mathrm{DFT}} \right]^2, \qquad (5)$$

where $E_{\mathrm{DFT}}^{\alpha}$ is the calculated total energy for the configuration α and $E_{\mathrm{DFT}}^{\mathrm{FM}}$ is the calculated total energy for the ferromagnetic configuration. Figure 11 also shows (as a line) the function $E = \sum_{l=1}^{6} (c_l^{\alpha} - 1) J_l M_S^2$ which illustrates the quality of the fitted exchange parameters J_l.

The obtained isotropic exchange couplings J_l are listed in Table IV. The largest values are in the meV range, which is consistent with the experimentally observed magnetic transition temperature T_{N}.

Except for J_4, all considered interactions are antiferromagnetic (negative J_l). The magnetic interactions in the **a** and **c** directions are the largest ones (J_3 along **c** and J_6 along **a**) which suggests that the magnetic configurations inside the (**a**, **c**) plane drive the magnetic properties of the crystal. This is supported by Fig. 11. Indeed, the calculated energies (colorful scatters) are gathered into groups that correspond to different (**a**, **c**)-plane configurations, independently of the ordering in the **b** direction.

The different magnetic patterns in the (**a**, **c**) planes are depicted in Fig. 12. As J_3 and J_6 are both antiferromagnetic and $|J_3| > |J_6|$, we expect $E_{\mathrm{AFMc\&}a} < E_{\mathrm{AFMc}} < E_{\mathrm{AFM}a} < E_{\mathrm{FM}}$. The energy order observed in Fig. 11 is perfectly consistent with this in-plane energy order.

In addition, we have evaluated an alternate Heisenberg model with all J_l except J_3 and J_6 (i.e., the *ac*-planar exchange couplings) set to zero (see the black lines in Fig. 11). Notably, this purely planar model is sufficient to describe

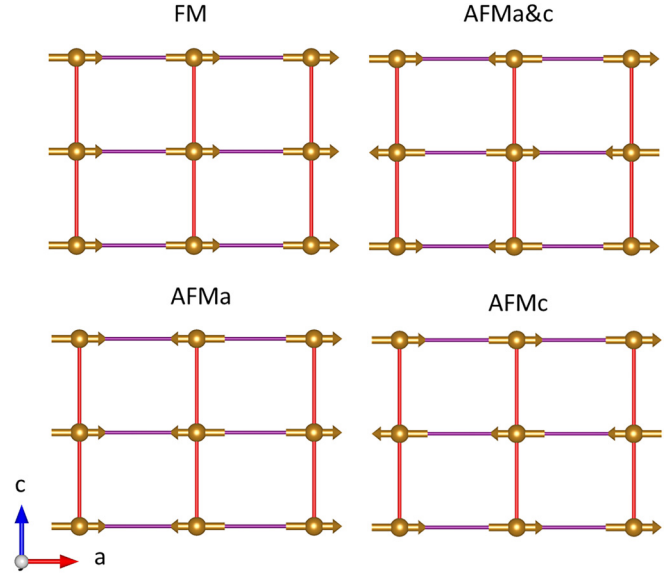

FIG. 12. Several possible magnetic configurations in the (**a**, **c**) plane. The red and purple lines correspond respectively to the interactions J_3 and J_6.

the different families of magnetic configurations with an acceptable accuracy. In other words, Li_2FeSiO_4 exhibits almost two-dimensional magnetism.

V. DISCUSSION AND SUMMARY

While the evolution of long-range antiferromagnetic order in Li_2FeSiO_4 at $T_{\mathrm{N}} = 17$ K is marked by sharp λ-like anomalies in the specific heat and $\partial(\chi_a T)/\partial T$, our experimental data also suggest the presence of short-range spin order at temperatures above $10 \times T_{\mathrm{N}}$. The presence of a broad maximum in the magnetic susceptibility well above the long-range ordering temperature is typical for low-dimensional antiferromagnetism and indicates the evolution of significant short-range magnetic order [43]. Both the observation of such a correlation maximum at 28 K and the fact that the Weiss temperature Θ exceeds T_{N} by a factor of $\simeq$3.5 [$T_{\mathrm{N}}/\Theta \simeq 0.27(2)$] suggest the low-dimensional nature of magnetism in Li_2FeSiO_4. This is supported by the observation of a reduced ordered moment $\mu = 2.50(2)\ \mu_{\mathrm{B}}$/Fe, at $T = 1.5$ K, obtained from neutron diffraction. Additionally, we find that magnetic anisotropy beyond g-factor anisotropy extends to temperatures up to about 200 K, i.e., more than $10 \times T_{\mathrm{N}}$, as well as significant nonphononic entropy changes up to at least 100 K. Since strong single-ion effects are rather unlikely in the high-spin Fe^{2+} system under study, we associate the observed anisotropy in χ with the evolution of short-range correlations presumably of magnetic nature. However our data do not exclude effects of orbital degrees of freedom either. The presence of short-range order up to at least 100 K is unambiguously evidenced by the measured nonphononic entropy changes. At 100 K, the magnetic entropy is still not fully released which agrees with the scenario of short-range magnetic order up to 200 K. The presence of short-range magnetic order well above T_{N} further corroborates the evidence of low-dimensional magnetism in Li_2FeSiO_4.

This conclusion of low-dimensional magnetism is fully confirmed by our numerical studies, where the magnetic couplings were estimated using the broken-symmetry formalism by minimizing total energies of various spin configurations and mapping onto the Heisenberg Hamiltonian. The experimentally observed antiferromagnetic spin configuration, as determined by our neutron diffraction experiment, is indeed found to exhibit nearly the lowest energy, supporting the validity of our approach. Our analysis yields as dominating magnetic exchange couplings $J_3 = -6.1$ K ($||c$ axis) and $J_6 = -1.7$ K ($||a$ axis) forming two-dimensional magnetic layers. While J_1 and J_5 are negligibly small, J_2 and J_4 provide finite interplanar coupling which, in combination with magnetic anisotropy, present derivations from the pure 2D Heisenberg case and, hence, drive long-range magnetic order. The antiferromagnetic interplane coupling $J_2 = -0.5$ K between adjacent layers of Fe^{2+} moments is frustrated so that the next-nearest-neighbor coupling $J_4 = 0.48$ K is given as leading interplane coupling. It is ferromagnetic which contradicts the observed spin structure. However, the error in the calculated value is rather large (due to the crushing driving role of J_3 and J_6 in the coupling) so that even its sign is subject to uncertainty. Hence, our numerical study does not rule out a small negative J_4 which would be consistent with the observed superstructure vector $\mathbf{k} = (\frac{1}{2}, 0, \frac{1}{2})$.

The high-spin nature of Fe^{2+} in Li_2FeSiO_4 is further confirmed by our Mössbauer data which imply a main magnetic Fe^{2+} site in the $S = 2$ state. The observed value of the asymmetry parameter of EFG underlines the relevance of the tetrahedral distortion for magnetism in Li_2FeSiO_4. The observed static magnetic hyperfine field of 14.8(3) T indicates significant orbital contributions to the hyperfine field. Notably, both the magnetic order parameter critical exponents as determined by neutron scattering and Mössbauer spectroscopy, i.e., $\beta^{\mathrm{PND}} = 0.185(10)$ and $\beta^{\mathrm{MB}} = 0.116(12)$, are much smaller than expected for three-dimensional magnetic systems where $\beta \simeq 0.33$ (3D Ising) and $\beta \simeq 0.35$–0.37 (3D Heisenberg, 3D XY) are found [44]. We emphasize, however, that β^{PND} only indirectly reflects the critical behavior as it is affected by the decrease of the magnetic volume fraction f_{mag} which, in the temperature regime between 13 and 17 K, continuously decreases from 0.9 to 0.2 so that I_{B} is suppressed by a factor $\sqrt{f_{\mathrm{mag}}}$ (see Fig. 7 and the detailed discussion in Sec. III C). The critical exponent $\beta^{\mathrm{MB}} = 0.116(12)$ observed by Mössbauer spectroscopy is similar to $\beta = 0.125$ of the 2D Ising model and suggests the two-dimensional nature of magnetism in Li_2FeSiO_4.

Since orbital degrees of freedom are relevant in JT-active high-spin Fe^{2+} in tetrahedral coordination with the electronic configuration $e_g^3 t_{2g}^3$, one may speculate whether a distinct orbital arrangement and/or orbital order is associated with the observed 2D nature of magnetism. The role of orbital magnetism is, e.g., relevant in the 2D Ising-type antiferromagnet $FePS_3$, where it leads to long-range antiferromagnetic order down to the monolayer limit [45]. As shown by the well-known examples $KCuF_3$ and $LaMnO_3$, particular orbital-ordered ground states are interconnected with specific (low-dimensional) magnetic structures [5–7]. This can even yield one-dimensional magnetic substructures in structurally layered systems, as seen in honeycomb-structured $A_3Cu_2SbO_6$ (A = Li, Na), where 1D magnetic substructures are formed due to the particular orbital arrangement [46,47].

In summary, we have solved the magnetic ground state of Li_2FeSiO_4 and report experimental and theoretical evidence of the quasi-2D nature of magnetism which is due to weak and partly frustrated interlayer coupling of the rectangular $S = 2$ Fe^{2+} magnetic lattice. Our works adds a system with high-spin tetrahedrally coordinated Fe^{2+} ions to the family of quasi-2D magnetic materials where in addition to spin also the orbital degree of freedom is relevant.

ACKNOWLEDGMENTS

We acknowledge support by Deutsche Forschungsgemeinschaft (DFG) under Germany's Excellence Strategy EXC2181/1-390900948 (the Heidelberg STRUCTURES Excellence Cluster) and the collaborative research center 1143 at TU Dresden. Beam time was provided by the Institut Laue-Langevin (Grenoble, France) under Proposal 5-31-2539 [17].

[1] C. Gong and X. Zhang, Two-dimensional magnetic crystals and emergent heterostructure devices, Science **363**, eaav4450 (2019).

[2] M. Imada, A. Fujimori, and Y. Tokura, Metal-insulator transitions, Rev. Mod. Phys. **70**, 1039 (1998).

[3] Y. Tokura and N. Nagaosa, Orbital physics in transition-metal oxides, Science **288**, 462 (2000).

[4] A. M. Oles, Charge and orbital order in transition metal oxides, Acta Phys. Pol. A **118**, 212 (2010).

[5] R. Caciuffo, L. Paolasini, A. Sollier, P. Ghigna, E. Pavarini, J. van den Brink, and M. Altarelli, Resonant x-ray scattering study of magnetic and orbital order in $KCuF_3$, Phys. Rev. B **65**, 174425 (2002).

[6] L. F. Feiner and A. M. Oleś, Electronic origin of magnetic and orbital ordering in insulating $LaMnO_3$, Phys. Rev. B **59**, 3295 (1999).

[7] J. Geck, P. Wochner, S. Kiele, R. Klingeler, P. Reutler, A. Revcolevschi, and B. Büchner, Orbital polaron lattice formation in lightly doped $La_{1-x}Sr_xMnO_3$, Phys. Rev. Lett. **95**, 236401 (2005).

[8] M. S. Islam, R. Dominko, C. Masquelier, C. Sirisopanaporn, A. R. Armstrong, and P. G. Bruce, Silicate cathodes for lithium batteries: Alternatives to phosphates? J. Mater. Chem. **21**, 9811 (2011).

[9] C. Sirisopanaporn, C. Masquelier, P. G. Bruce, A. R. Armstrong, and R. Dominko, Dependence of Li_2FeSiO_4 electrochemistry on structure, J. Am. Chem. Soc. **133**, 1263 (2011).

[10] J. Yang, J. Zheng, X. Kang, G. Teng, L. Hu, R. Tan, K. Wang, X. Song, M. Xu, S. Mu, and F. Pan, Tuning structural stability and lithium-storage properties by d-orbital hybridization substitution in full tetrahedron Li_2FeSiO_4 nanocrystal, Nano Energy **20**, 117 (2016).

[11] X. Lu, H. Wei, H.-C. Chiu, R. Gauvin, P. Hovington, A. Guerfi, K. Zaghib, and G. Demopoulos, Rate-dependent phase transitions in Li_2FeSiO_4 cathode nanocrystals, Sci. Rep. **5**, 8599 (2015).

[12] S.-i. Nishimura, S. Hayase, R. Kanno, M. Yashima, N. Nakayama, and A. Yamada, Structure of Li_2FeSiO_4, J. Am. Chem. Soc. **130**, 13212 (2008).

[13] A. Boulineau, C. Sirisopanaporn, R. Dominko, A. R. Armstrong, P. G. Bruce, and C. Masquelier, Polymorphism and structural defects in Li_2FeSiO_4, Dalton Trans. **39**, 6310 (2010).

[14] W. Hergett, M. Jonak, J. Werner, F. Billert, S. Sauerland, C. Koo, C. Neef, and R. Klingeler, Synthesis and magnetism of a Li_2FeSiO_4 single crystal, J. Magn. Magn. Mater. **477**, 1 (2019).

[15] W. Hergett, C. Neef, H. Wadepohl, H.-P. Meyer, M. M. Abdel-Hafiez, C. Ritter, E. Thauer, and R. Klingeler, High-pressure optical floating-zone growth of Li_2FeSiO_4 single crystals, J. Cryst. Growth **515**, 37 (2019).

[16] W. Hergett, C. Neef, H.-P. Meyer, and R. Klingeler, Challenges in the crystal growth of Li_2FeSiO_4, J. Cryst. Growth **556**, 125995 (2021).

[17] W. Hergett, S. Spachmann, C. Neef, M. Enderle, C. Ritter, and R. Klingeler, Crystal and magnetic structure of *Pmnb*-Li_2FeSiO_4, Institut Laue-Langevin (ILL), doi:10.5291/ILL-DATA.5-31-2539.

[18] J. Rodríguez-Carvajal, Recent advances in magnetic structure determination by neutron powder diffraction, Phys. B (Amsterdam, Neth.) **192**, 55 (1993).

[19] J. Rodríguez-Carvajal, BASIREPS: A program for calculating irreducible representations of space groups and basis functions for axial and polar vector properties, part of the FULLPROF suite of programs, https://www.ill.eu/sites/fullprof.

[20] K. Momma and F. Izumi, *VESTA3* for three-dimensional visualization of crystal, volumetric and morphology data, J. Appl. Crystallogr. **44**, 1272 (2011).

[21] S. Kamusella and H.-H. Klauss, Moessfit: A free Mössbauer fitting program, Hyperfine Interact. **237**, 82 (2016).

[22] K. Koepernik and H. Eschrig, Full-potential nonorthogonal local-orbital minimum-basis band-structure scheme, Phys. Rev. B **59**, 1743 (1999).

[23] I. Opahle, K. Koepernik, and H. Eschrig, Full-potential band-structure calculation of iron pyrite, Phys. Rev. B **60**, 14035 (1999).

[24] J. P. Perdew and Y. Wang, Accurate and simple analytic representation of the electron-gas correlation energy, Phys. Rev. B **45**, 13244 (1992).

[25] H. Eschrig, K. Koepernik, and I. Chaplygin, Density functional application to strongly correlated electron systems, J. Solid State Chem. **176**, 482 (2003).

[26] See Supplemental Material at http://link.aps.org/supplemental/10.1103/PhysRevB.111.024414 for additional magnetization data.

[27] J. Krzystek, A. Ozarowski, and J. Telser, Multi-frequency, high-field EPR as a powerful tool to accurately determine zero-field splitting in high-spin transition metal coordination complexes, Coord. Chem. Rev. **250**, 2308 (2006).

[28] P. Gibart, J.-L. Dormann, and Y. Pellerin, Magnetic properties of $FeCr_2S_4$ and $CoCr_2S_4$, Phys. Status Solidi B **36**, 187 (1969).

[29] V. Fritsch, J. Hemberger, N. Büttgen, E.-W. Scheidt, H.-A. Krug von Nidda, A. Loidl, and V. Tsurkan, Spin and orbital frustration in $MnSc_2S_4$ and $FeSc_2S_4$, Phys. Rev. Lett. **92**, 116401 (2004).

[30] Z. Gong and Y. Yang, Recent advances in the research of polyanion-type cathode materials for Li-ion batteries, Energy Environ. Sci. **4**, 3223 (2011).

[31] M. Bini, S. Ferrari, C. Ferrara, M. Mozzati, D. Capsoni, A. Pell, G. Pintacuda, and P. Canton, Polymorphism and magnetic properties of Li_2MSiO_4 (M = Fe, Mn) cathode materials, Sci. Rep. **3**, 3452 (2013).

[32] K. Zaghib, A. Salah, N. Ravet, A. Mauger, F. Gendron, and C. Julien, Structural, magnetic and electrochemical properties of lithium iron orthosilicate, J. Power Sources **160**, 1381 (2006).

[33] J. Werner, C. Neef, C. Koo, S. Zvyagin, A. Ponomaryov, and R. Klingeler, Antisite disorder in the battery material $LiFePO_4$, Phys. Rev. Mater. **4**, 115403 (2020).

[34] C. Neef, H. Wadepohl, H.-P. Meyer, and R. Klingeler, High-pressure optical floating-zone growth of Li(Mn,Fe)PO_4 single crystals, J. Cryst. Growth **462**, 50 (2017).

[35] U. Köbler, One-dimensional boson fields in the critical range of EuS and EuO, Acta Phys. Pol. A **128**, 398 (2015).

[36] Y.-L. Chen and D.-P. Yang, Hyperfine interactions, in *Mössbauer Effect in Lattice Dynamics* (John Wiley & Sons, 2007), Chap. 2, pp. 29–77.

[37] P. Imbert, F. Varret, and M. Wintenberger, Etude par effet Mössbauer de la briartite (Cu_2FeGeS_4), J. Phys. Chem. Solids **34**, 1675 (1973).

[38] A. Saúl and G. Radtke, Magnetic couplings in CsV_2O_5: A new picture, Phys. Rev. Lett. **106**, 177203 (2011).

[39] A. Saúl and G. Radtke, Density functional approach for the magnetism of β-$TeVO_4$, Phys. Rev. B **89**, 104414 (2014).

[40] E. A. Zvereva, M. I. Stratan, Y. A. Ovchenkov, V. B. Nalbandyan, J.-Y. Lin, E. L. Vavilova, M. F. Iakovleva, M. Abdel-Hafiez, A. V. Silhanek, X.-J. Chen, A. Stroppa, S. Picozzi, H. O. Jeschke, R. Valentí, and A. N. Vasiliev, Zigzag antiferromagnetic quantum ground state in monoclinic honeycomb lattice antimonates $A_3Ni_2SbO_6$ (A = Li, Na), Phys. Rev. B **92**, 144401 (2015).

[41] K. Foyevtsova, I. Opahle, Y.-Z. Zhang, H. O. Jeschke, and R. Valentí, Determination of effective microscopic models for the frustrated antiferromagnets Cs_2CuCl_4 and Cs_2CuBr_4 by density functional methods, Phys. Rev. B **83**, 125126 (2011).

[42] Wolfram, Inc., Mathematica, Version 11.3, Champaign, IL, 2018.

[43] L. de Jongh and A. Miedema, Experiments on simple magnetic model systems, Adv. Phys. **23**, 1 (1974).

[44] A. Pelissetto and E. Vicari, Critical phenomena and renormalization-group theory, Phys. Rep. **368**, 549 (2002).

[45] X. Wang, K. Du, F. Liu, P. Hu, J. Zhang, Q. Zhang, M. Owen, X. Lu, C. Gan, P. Sengupta, C. Kloc, and Q. Xiong, Raman spectroscopy of atomically thin two-dimensional magnetic iron phosphorus trisulfide ($FePS_3$) crystals, 2D Mater. **3**, 031009 (2016).

[46] M. Schmitt, O. Janson, S. Golbs, M. Schmidt, W. Schnelle, J. Richter, and H. Rosner, Microscopic magnetic modeling for the $S = \frac{1}{2}$ alternating-chain compounds $Na_3Cu_2SbO_6$ and $Na_2Cu_2TeO_6$, Phys. Rev. B **89**, 174403 (2014).

[47] C. Koo, E. Zvereva, I. Shukaev, M. Richter, M. Stratan, A. Vasiliev, V. Nalbandyan, and R. Klingeler, Static and dynamic magnetic response of fragmented Haldane-like spin chains in layered $Li_3Cu_2SbO_6$, J. Phys. Soc. Jpn. **85**, 084702 (2016).